

Discrete Linear Canonical Transform on Graphs: Uncertainty Principles and Sampling

Yu Zhang and Bing-Zhao Li*, *Member, IEEE*,

Abstract—With an increasing influx of classical signal processing methodologies into the field of graph signal processing, approaches grounded in discrete linear canonical transform have found application in graph signals. In this paper, we initially propose the uncertainty principle of the graph linear canonical transform (GLCT), which is based on a class of graph signals maximally concentrated in both vertex and graph spectral domains. Subsequently, leveraging the uncertainty principle, we establish conditions for recovering bandlimited signals of the GLCT from a subset of samples, thereby formulating the sampling theory for the GLCT. We elucidate interesting connections between the uncertainty principle and sampling. Further, by employing sampling set selection and experimental design sampling strategies, we introduce optimal sampling operators in the GLCT domain. Finally, we evaluate the performance of our methods through simulations and numerical experiments across applications.

Index Terms—Graph signal processing, graph linear canonical transform, uncertainty principle, sampling theory.

I. INTRODUCTION

ADVANCEMENTS in information and communication technologies have led to the integration of various types of data in fields such as social networks, recommendation systems, medical image processing, and bioinformatics. Unlike traditional time series or digital images, these datasets often exhibit complex and irregular structures, posing challenges for conventional signal processing tools [1], [2]. Over the past decade, significant progress has been made in the development of tools for analyzing signals defined on graphs, giving rise to the field of graph signal processing (GSP) [1]–[6].

GSP relies on graph topology, extending traditional discrete signal processing to signals characterized by the complex and irregular underlying structures represented by corresponding graphs. Emphasizing the relationship, interaction, and effects between signals and their graph structures in various real-world scenarios, GSP aims to build a theoretical framework for high-dimensional and large-scale data analysis tasks from a signal processing perspective. This includes graph transforms [1]–[4], [7], [8], frequency analysis [9], [10], filtering [11], [12], sampling and interpolation [13]–[18], reconstruction and

recovery [19]–[21], uncertainty principles on graphs [14], [22], [23], fast computation algorithms [15], [24], and more. In GSP, spectral analysis plays a crucial role, inspired by harmonic analysis, using the graph Laplacian operator as its core theoretical foundation, naturally extending concepts such as frequency and filter banks to the graph domain [1], [3]. On the other hand, inspired by algebraic methods, the multiplication of the graph signal with the adjacency matrix of the underlying graph yields the fundamental shift operation for graph signals [2], [4]. These two approaches bring complementary perspectives and tools, collectively fostering attention and development in the GSP field. In this paper, we adopt an algebraic method framework to broaden its scope.

A crucial tool in this framework is the graph Fourier transform (GFT), which expands signals into eigenvectors of the adjacency matrix, defining the spectrum through corresponding eigenvalues. It is a direct generalization of the discrete Fourier transform to graphs [4]. Although the GFT can perform various operations on real-world graph signals, it cannot capture the transformation process from the vertex domain to the spectral domain and cannot handle graph signals with chirp-like characteristics [25], [26]. In recent years, approaches like windowed graph Fourier transform [10], graph fractional Fourier transform (GFRFT) [25], windowed graph fractional Fourier transform [27], and the directed graph fractional Fourier transform [28] have been proposed to address issues with these methods. However, these approaches still suffer from insufficient degrees of freedom, lack of flexibility, and underutilization of parameters. In our previous study [29], we extended the linear canonical transform (LCT) [30] to graphs, introducing the graph linear canonical transform (GLCT). As the generalization of the Fourier transform and fractional Fourier transform, the GLCT, with its three free parameters, exhibits strong adaptability and flexibility in signal processing. It demonstrates clear advantages in handling non-stationary signals and non-integer-order cases. We prove that it satisfies all expected properties, unifying GFT, GFRFT, and graph scale transform, and provide two examples of GLCT.

In this paper, we further explore the uncertainty principle in the GLCT domain. The Heisenberg uncertainty principle in continuous-time signals [31], highlights the fundamental trade-off between the signal's spread in time and its spread in frequency. Specifically, continuous-time signals cannot be perfectly localized in both time and frequency domains. In [22], the uncertainty principle for graph signals was first introduced using geodesic distance, aiming to establish a connection between the signal spread at the vertices of the graph and its spectrum spread defined by GFT in the graph

This paper was supported by the National Natural Science Foundation of China [No. 62171041], the BIT Research and Innovation Promoting Project [No.2023YCX053], and Beijing Municipal Natural Science Foundation [No. 4242011]. Corresponding author: Bing-Zhao Li.

Y. Zhang is with School of Mathematics and Statistics, Beijing Institute of Technology, Beijing 102488, China and also with the Department of Mechanical Engineering, Keio University, Yokohama 223-8522, Japan (e-mail: zhangyu_bit@keio.jp).

B. Z. Li is with School of Mathematics and Statistics, Beijing Institute of Technology, Beijing 102488, China (e-mail: li_bingzhao@bit.edu.cn).

spectral domain. However, a key difference between graph signals and time signals is that, while time or frequency has a well-defined distance concept, graphs are not metric spaces. Additionally, the vertices of a graph can represent more complex signals, such as those in Hilbert spaces [32]. To overcome the complexity of defining distances, M. Tsitsvero, and others [14] creatively introduced prolate spheroidal wave functions [33], [34] into graph signals, defining a new graph uncertainty principle using the energy percentage. We leverage this approach to derive the uncertainty principle in the GLCT domain.

Furthermore, based on the proposed uncertainty principles of GLCT and its localization properties, we consider sampling and reconstruction in the GLCT domain. In [13], it was demonstrated that bandlimited graph signals can be perfectly recovered with a sufficient number of samples. There is an intriguing connection between sampling theory and uncertainty principles in the GLCT domain, leading to conditions for recovering bandlimited signals from subsets of their values. These conditions are found to be equivalent to those derived in [13], [14], [35]. We present several signal recovery algorithms and sampling strategies aimed at finding the optimal sampling set. Building on the relationship between the GFT, the GFRFT and, the GLCT, this paper establishes a framework for graph signal sampling based on prior information in the GLCT domain. The sampling process can be viewed as a filtering operation in the GLCT domain, and the choice of filters allows the reconstruction of graph signals.

Our contributions are summarized as follows:

- Firstly, based on conditions for perfect localization in the vertex and graph spectral domains, we propose an uncertainty principle in the GLCT domain and discuss its intriguing connection with sampling.
- Secondly, by defining bandlimited signals in the GLCT domain, we propose conditions for sampling and perfect recovery in the GLCT domain. We present a method for designing and selecting optimal sampling operators from qualified sampling operators, comparing various sampling strategies.
- Finally, through simulation experiments, we compare our proposed sampling framework with GFT and GFRFT approaches. The results demonstrate that our sampling framework produces minimal errors and showcases its competitive performance in the application of semi-supervised classification for online blogs and clustering of IEEE 118 bus test cases.

This paper is structured as follows. Section II provides a brief overview of our prior work in [29], the graph uncertainty principle, and the graph sampling framework. In Section III, based on conditions for perfect localization, we propose uncertainty principles in the GLCT domain and discuss their relationship with sampling. In Section IV, we begin by defining M-bandlimited signals, introduce conditions for sampling and perfect recovery in the GLCT domain, and select the optimal sampling operator from qualified sampling operators. We present various sampling strategies and compare them. Section V evaluates the classification performance of GLCT

sampling on online blogs and clustering of IEEE 118 bus test cases, comparing it with GFT and GFRFT sampling. Finally, Section VI concludes this paper.

II. PRELIMINARIES

In this section, we briefly review concepts in discrete signal processing on GLCT [29] and introduce the uncertainty principle of graph signals [22] and the basic theory of sampling [13], [14].

A. Graph Linear Canonical Transform

In discrete signal processing on graphs, the high-dimensional structure of a signal is represented by a graph $\mathcal{G} = (\mathcal{V}, \mathbf{A})$, where $\mathcal{V} = v_0, \dots, v_{N-1}$ denotes the set of vertices and $\mathbf{A} \in \mathbb{C}^{N \times N}$ denotes the weighted adjacency matrix. The graph signal is defined as a mapping that maps the vertex v_n to a signal coefficient $x_n \in \mathbb{C}$, which can also be written as a complex vector

$$\mathbf{x} = [x_0 \ x_1 \ \dots \ x_{N-1}]^\top \in \mathbb{C}^N.$$

Graph Fourier transform (GFT) [1]–[4] is defined by the eigendecomposition of an adjacency matrix

$$\mathbf{A} = \mathbf{V} \mathbf{\Lambda}_\mathbf{A} \mathbf{V}^{-1} = \sum_{i=0}^{N-1} \lambda_{\mathbf{A}_i} u_i u_i^*, \quad (1)$$

where the columns u_0, u_1, \dots, u_{N-1} of \mathbf{V} are the eigenvectors of \mathbf{A} , and the eigenvalues in the corresponding diagonal matrix $\mathbf{\Lambda}_\mathbf{A} \in \mathbb{C}^{N \times N}$ are $\lambda_{\mathbf{A}_0}, \dots, \lambda_{\mathbf{A}_{N-1}}$. The GFT is defined as $\hat{\mathbf{x}} = \mathbf{V}^{-1} \mathbf{x}$.

Definition 1. *Parallel to the GFT, the GLCT of $\mathbf{x} \in \mathbb{C}^N$ can be defined as*

$$\hat{\mathbf{x}} = \mathbf{O}^\mathbf{M} \cdot \mathbf{x} = \{ \mathbf{\Lambda}^\xi \mathbf{Q}_\sigma \mathbf{\Lambda}^\alpha \mathbf{Q}^\top \} \mathbf{x}, \quad (2)$$

where the operator $\mathbf{O}^\mathbf{M}$ is an operator of the GLCT, and the matrix \mathbf{M} entries are $(a, b; c, d)$, which is called a GLCT parameter matrix, and $ad - bc = 1$, $a, b, c, d \in \mathbb{R}$. The $\mathbf{\Lambda}^\xi$ matrix, \mathbf{Q}_σ matrix, and $\mathbf{\Lambda}^\alpha$ matrix are the matrices in the graph chirp multiplication (CM), graph scale transform, and graph fractional Fourier transform (GFRFT), respectively [29].

The matrices \mathbf{Q} and $\mathbf{\Lambda}$ are given by the spectral decomposition of the GFT matrix $\mathbf{V}^{-1} = \mathbf{Q} \mathbf{\Lambda} \mathbf{Q}^{-1}$, which is orthogonal and diagonalized. Furthermore, its inverse GLCT (IGLCT) is

$$\mathbf{x} = \mathbf{O}^{-\mathbf{M}} \cdot \hat{\mathbf{x}} = \{ \mathbf{Q} \mathbf{\Lambda}^{-\alpha} \mathbf{Q}_\sigma^\top \mathbf{\Lambda}^{-\xi} \} \hat{\mathbf{x}}. \quad (3)$$

The parameter relations between \mathbf{M} and (ξ, σ, α) are

$$\begin{aligned} \xi &= \frac{ac + bd}{a^2 + b^2}, \quad \sigma = \sqrt{a^2 + b^2}, \\ \alpha &= \arccos\left(\frac{a}{\sigma}\right) = \arcsin\left(\frac{b}{\sigma}\right). \end{aligned} \quad (4)$$

Remark 1. *In particular, when $a = \cos \alpha, b = \sin \alpha, c = -\sin \alpha$, and $d = \cos \alpha$, the GLCT operator will be the GFRFT operator [25], when $a = 0, b = 1, c = -1$, and $d = 0$, the GLCT operator will be the GFT operator.*

B. Graph Uncertainty Principle

A fundamental property of signals is the Heisenberg uncertainty principle [31], which states that there is a fundamental trade-off between the spread of a signal in time and the spread of its spectrum in frequency. the traditional uncertainty principle of time signals is

$$\Delta t^2 \Delta \omega^2 \geq \frac{1}{4},$$

where Δt^2 and $\Delta \omega^2$ denote the time and frequency spreads, respectively, of the classical continuous-time signal $x(t)$ and its Fourier domain counterpart $\hat{x}(\omega)$.

After the GFT was proposed, the signal uncertainty principle defined on undirected connected graphs was first derived in [22]. The spreads of vector \mathbf{x} in the vertex domain and the GFT domain are respectively defined as

$$\begin{cases} \Delta g^2 := \min_{u_0 \in \mathcal{V}} \frac{1}{\|\mathbf{x}\|^2} \mathbf{x}^* \mathbf{P}_{u_0}^2 \mathbf{x}, \\ \Delta s^2 := \frac{1}{\|\mathbf{x}\|^2} \sum_i \lambda_{\mathbf{A}_i} |\hat{\mathbf{x}}_i|^2, \end{cases} \quad (5)$$

where $\mathbf{P}_{u_0} := \text{diag}(d(u_0, v_1), d(u_0, v_2), \dots, d(u_0, v_N))$, and $d(u, v)$ denotes the geodesic distance between nodes u and v . Thus, the graph uncertainty principle can be represented by the admissible region of Δg^2 and Δs^2 , i.e.,

$$\Gamma_{u_0} = \{(s, g) : \Delta s^2(\mathbf{x}) = s, \Delta g_{u_0}^2(\mathbf{x}) = g\},$$

and the curve can be expressed as

$$\gamma_{u_0} = \min_{\mathbf{x}} \Delta g_{u_0}^2(\mathbf{x}) \text{ subject to } \Delta s^2(\mathbf{x}) = s.$$

The above uncertainty principle studies the trade-off between the graph signal distribution and its spectral domain based on the specific definition of graph distances. However, a key distinction between the graph signal and the time signal is that time exists in a metric space with a well-defined distance concept, whereas the graph is not metric space, and its vertices can be more complex. In this case, defining distances between vertices is not straightforward.

To overcome the limitations associated with graph distance definitions, this paper adopts an alternative definition based on spread [14]. We derive an uncertainty principle for the GLCT domain that does not require any additional distance definitions.

This method characterizes temporal spread based on the percentage of energy falling within the interval $[-T/2, T/2]$, defined as

$$\frac{\int_{-T/2}^{T/2} |x(t)|^2 dt}{\int_{-\infty}^{+\infty} |x(t)|^2 dt} = \zeta^2. \quad (6)$$

Similarly, the definition of frequency domain spread is given by

$$\frac{\int_{-W/2}^{W/2} |\hat{x}(\omega)|^2 d\omega}{\int_{-\infty}^{+\infty} |\hat{x}(\omega)|^2 d\omega} = \eta^2. \quad (7)$$

Using these two defined spreads, we can further study the uncertainty principle in the GLCT domain in Section III.

C. Sampling on Graph Signals

Sampling is one of the fundamental challenges in GSP. Its objective is to identify conditions for recovering bandlimited graph signals from a subset of values and to devise suitable sampling and recovery strategies [14].

Consider the sampling set $\mathcal{S} = (\mathcal{S}_0, \dots, \mathcal{S}_{|\mathcal{S}|-1})$, $\mathcal{S}_i \in \{0, 1, \dots, N-1\}$, its dimension coefficient is defined as $|\mathcal{S}|$. This coefficient is the size of the sampling indexes for obtaining a sampled signal $\mathbf{x}_{\mathcal{S}} \in \mathbb{C}^{|\mathcal{S}|}$ ($|\mathcal{S}| < N$) from a bandlimited graph signal $\mathbf{x} \in \mathbb{C}^N$. The sampling operator \mathbf{D} is defined as a linear mapping from \mathbb{C}^N to $\mathbb{C}^{|\mathcal{S}|}$ [13], which is expressed as

$$\mathbf{D}_{i,j} = \begin{cases} 1, & j = \mathcal{S}_i, \\ 0, & \text{otherwise.} \end{cases} \quad (8)$$

We then recover \mathbf{x} from $\mathbf{x}_{\mathcal{S}}$ with interpolation operator \mathbf{R} , which is a linear mapping from $\mathbb{C}^{|\mathcal{S}|}$ to \mathbb{C}^N .

$$\begin{aligned} \text{sampling : } \quad \mathbf{x}_{\mathcal{S}} &= \mathbf{D}\mathbf{x} \in \mathbb{C}^{|\mathcal{S}|}, \\ \text{interpolation : } \quad \mathbf{x}_{\mathcal{R}} &= \mathbf{R}\mathbf{x}_{\mathcal{S}} = \mathbf{R}\mathbf{D}\mathbf{x} \in \mathbb{C}^N, \end{aligned}$$

where $\mathbf{x}_{\mathcal{R}} \in \mathbb{C}^N$ recovers \mathbf{x} either approximately or exactly.

III. UNCERTAINTY PRINCIPLE IN THE GLCT DOMAIN

In the realm of continuous-time signals, Landau, Pollak, and Slepian extensively explored space-frequency analysis linked to projection operators. Their groundbreaking work, spanning the 1960s, encompassed the uncertainty principle, eigenvalue distributions, and prolate ellipsoid wave functions [33], [34]. By extending this uncertainty principle to graph signals [14], we circumvent the need for any extra distance definition, mitigating the drawbacks associated with graph distance definitions. Furthermore, we apply this methodology to establish the uncertainty principle in the GLCT domain.

A. Localization in Vertex and Spectral Domains

Before defining the uncertainty principle, we first introduce two localization (bandlimited) operators [36]. For a subset of vertices $\mathcal{S} \subseteq \mathcal{V}$, the *vertex-limiting* operator is defined as follows

$$\mathbf{D}_{\mathcal{S}} = \text{diag}(d_1, \dots, d_i, \dots, d_N), \quad (9)$$

where, $d_i = 1$, if $i \in \mathcal{S}$, and $d_i = 0$ if $i \notin \mathcal{S}$, $i = 1, \dots, N$. For this operator, it is the corresponding sampling operator $\mathbf{D}_{\mathcal{S}}$ in (8).

Similarly, given the unitary matrix \mathbf{O}^M used in (2) and the index subset $\mathcal{F} \subseteq \hat{\mathcal{G}}$, where $\hat{\mathcal{G}} = \{1, \dots, N\}$ represents the set of all graph spectral indices, we introduce the *spectral-limiting* operator as

$$\mathbf{B}_{\mathcal{F}}^M = \mathbf{O}^{-M} \mathbf{\Sigma}_{\mathcal{F}} \mathbf{O}^M, \quad (10)$$

where, $\mathbf{\Sigma}_{\mathcal{F}}$ is a diagonal matrix whose definition is consistent with $\mathbf{D}_{\mathcal{S}}$, i.e. $\Sigma_{ii} = 1$, if $i \in \mathcal{F}$, and $\Sigma_{ii} = 0$ if $i \notin \mathcal{F}$.

According to the properties of diagonal matrices, it is evident that the operators $\mathbf{D}_{\mathcal{S}}$ and $\mathbf{B}_{\mathcal{F}}^M$ are symmetric and positive semi-definite, with a spectral norm of exactly 1 for both operators. To simplify notation without loss of generality, we use \mathbf{D} and \mathbf{B}^M to represent these two operators, respectively.

Therefore, the vector \mathbf{x} is perfectly localized (bandlimited) over \mathcal{S} if

$$\mathbf{D}\mathbf{x} = \mathbf{x}, \quad (11)$$

and perfectly localized (bandlimited) over \mathcal{F} if

$$\mathbf{B}^M \mathbf{x} = \mathbf{x}. \quad (12)$$

Here we have a lemma [14] about perfect localization.

Lemma 1. *A vector \mathbf{x} is perfectly localized over both the vertex set \mathcal{S} and the spectral set \mathcal{F} if and only if*

$$\lambda_{\max}(\mathbf{B}^M \mathbf{D} \mathbf{B}^M) = 1. \quad (13)$$

In such a case, \mathbf{x} is the eigenvector associated with the unit eigenvalue.

Proof. The proof is reported in Appendix A. \square

Equivalently, the perfect localization over sets \mathcal{S} and \mathcal{F} can also be achieved if and only if

$$\|\mathbf{B}^M \mathbf{D}\|_2 = \|\mathbf{D} \mathbf{B}^M\|_2 = 1. \quad (14)$$

B. Uncertainty Principle of the GLCT

Using the energy expectations of equations (6) and (7), we can extend them to the GLCT domain similar to [14], [23].

Suppose a vector \mathbf{x} , vertex subset \mathcal{S} , and graph spectral subset \mathcal{F} , two subsets are used (9) and (10). The vectors $\mathbf{D}\mathbf{x}$ and $\mathbf{B}^M \mathbf{x}$ represent the projection of \mathbf{x} on the vertex set \mathcal{S} and the spectral set \mathcal{F} respectively. Then, similar to equations (6) and (7), ζ^2 and $(\eta^M)^2$ are used to denote the energy expectations falling within the sets \mathcal{S} and \mathcal{F} respectively, as follows

$$\frac{\|\mathbf{D}\mathbf{x}\|_2^2}{\|\mathbf{x}\|_2^2} = \zeta^2, \quad \frac{\|\mathbf{B}^M \mathbf{x}\|_2^2}{\|\mathbf{x}\|_2^2} = (\eta^M)^2. \quad (15)$$

In this paper, we find closed-form region boundaries for all admissible pairs $\phi(\zeta, \eta^M)$ by generalizing the uncertainty principle of the GFT to the case of the GLCT. In (15), the graph topology is captured by the matrix \mathbf{O}^M , which appears in the definition of the GLCT in (2), inside the operator \mathbf{B}^M . Our goal is to establish a trade-off between ζ and η^M by localizing operators \mathbf{D} and \mathbf{B}^M , and find a signal that obtains all admissible pairs to prove the uncertainty principle.

If $\lambda_{\max}(\mathbf{B}^M \mathbf{D} \mathbf{B}^M) < 1$, we can though as the admissible region Γ provides clear bounds for specifying this uncertainty relation on \mathcal{G} .

Lemma 2. *Suppose for a vector \mathbf{x} , there are $\|\mathbf{x}\|_2 = 1$, $\|\mathbf{D}\mathbf{x}\|_2 = \zeta$, $\|\mathbf{B}^M \mathbf{x}\|_2 = \eta^M$, and $\lambda_{\max} < 1$ and if $\lambda_{\max} \leq \zeta^2 \eta^2$, there is an inequality*

$$\arccos \zeta + \arccos \eta^M \geq \arccos \sqrt{\lambda_{\max}(\mathbf{B}^M \mathbf{D} \mathbf{B}^M)}, \quad (16)$$

and finally reached the upper bound

$$\eta^M \leq \zeta \sqrt{\lambda_{\max}} + \sqrt{(1 - \zeta^2)(1 - \lambda_{\max})}. \quad (17)$$

Proof. The proof is reported in Appendix B. \square

Lemma 2 provides a general restriction on the set $\phi(\zeta, \eta^M)$ in the upper right corner of the unit square $[\lambda_{\max}, 1]^2$. By

simple generalization extension, we obtain similar results for the other three corners. For a subset \mathcal{S} , we denote its complement as $\bar{\mathcal{S}}$ such that $\mathcal{V} = \mathcal{S} \cup \bar{\mathcal{S}}$ and $\mathcal{S} \cap \bar{\mathcal{S}} = \emptyset$. Accordingly, we define the vertex projection on $\bar{\mathcal{S}}$ as $\bar{\mathbf{D}}$. Similarly, the projection on the complement $\bar{\mathcal{F}}$ is denoted by $\bar{\mathbf{B}}^M$. Considering all subdomains of the square $[0, 1]^2$, we obtain the uncertainty principle for the GLCT.

Theorem 1. *There exists a vector \mathbf{x} such that $\|\mathbf{x}\|_2 = 1$, $\|\mathbf{D}\mathbf{x}\|_2 = \zeta$, $\|\mathbf{B}^M \mathbf{x}\|_2 = \eta^M$, thus the admissible pair $\phi(\zeta, \eta^M) \in \Gamma$ is obtained, where*

$$\begin{aligned} \Gamma = \left\{ \phi(\zeta, \eta^M) : \arccos \zeta + \arccos \eta^M \right. \\ \geq \arccos \sqrt{\lambda_{\max}(\mathbf{B}^M \mathbf{D} \mathbf{B}^M)}, \\ \arccos \sqrt{1 - \zeta^2} + \arccos \eta^M \\ \geq \arccos \sqrt{\lambda_{\max}(\bar{\mathbf{B}}^M \bar{\mathbf{D}} \bar{\mathbf{B}}^M)}, \\ \arccos \zeta + \arccos \sqrt{1 - (\eta^M)^2} \\ \geq \arccos \sqrt{\lambda_{\max}(\bar{\mathbf{B}}^M \bar{\mathbf{D}} \bar{\mathbf{B}}^M)}, \\ \arccos \sqrt{1 - \zeta^2} + \arccos \sqrt{1 - (\eta^M)^2} \\ \left. \geq \arccos \sqrt{\lambda_{\max}(\bar{\mathbf{B}}^M \bar{\mathbf{D}} \bar{\mathbf{B}}^M)} \right\} \end{aligned} \quad (18)$$

Proof. The proof follows a similar structure to that of **Lemma 2**, demonstrating the inequalities for the remaining three corners. \square

Fig. 1 illustrates the uncertainty principle of **Theorem 1**, highlighting some noteworthy characteristics. The blue portion in the figure corresponds to the range of Γ in the GFT domain, while in the GLCT domain, the ranges in the lower left and upper right respectively tend to $(0, 0)$ and $(1, 1)$ as the parameter continuously changes, as indicated by the additional red portion. If we set the inequalities given by **Theorem 1** to equality, we can determine the equations of the curve at the four corners of Fig. 1, namely the upper right, upper left, lower right, and lower left corners. Notably, the upper right corner of the admissible region Γ specifies the domain where the maximum energy concentration occurs in the vertex and graph spectral for $\phi(\zeta, \eta^M)$. The equation for this curve is obtained

$$\begin{aligned} \eta^M = & \sqrt{\lambda_{\max}(\mathbf{B}^M \mathbf{D} \mathbf{B}^M)} \zeta \\ & + \sqrt{1 - \lambda_{\max}(\mathbf{B}^M \mathbf{D} \mathbf{B}^M)} \sqrt{1 - \zeta^2}. \end{aligned} \quad (19)$$

When the sets \mathcal{S} and \mathcal{F} yield matrices \mathbf{D} and \mathbf{B}^M satisfying the perfect localization condition in **Lemma 1**, the curve collapses to a single point, precisely in the upper right corner. Consequently, similar to [14], [23], any curve originating from a corner of the admissible region Γ in Fig. 1 can be mapped onto the corresponding corner, provided that the associated operator meets the criterion for perfect localization.

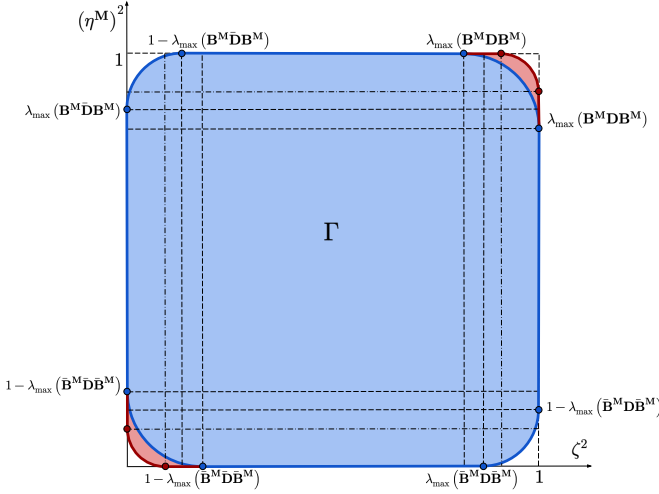


Fig. 1: The admissible region Γ in Theorem 1.

C. The Connection between the Uncertainty Principle and Sampling

For the proposed uncertainty principle and as described in [23], there are intriguing connections with the sampling conditions. Examining the upper left corner of the admissible region in Fig. 1, it is evident that if the signal is perfectly localized in the graph spectral subset \mathcal{F} , then $(\eta^M)^2 = 1$. However, for the vertex domain subset \mathcal{S} , we require $\zeta^2 \neq 0$ to avoid perfect localization of the signal on the complement of \mathcal{S} , making it unrecoverable. This is analogous to the perfect recovery conditions given in Section IV.

If we allow for some energy dissipation in the graph spectral domain, i.e., $(\eta^M)^2 < 1$, to ensure $\zeta^2 \neq 0$, we need to check

$$1 - \lambda_{\max}(\mathbf{B}^M \bar{\mathbf{D}} \mathbf{B}^M) > (\eta^M)^2.$$

This form of the condition is highly useful for designing potential sampling strategies, as it suggests using $\lambda_{\max}(\mathbf{B}^M \bar{\mathbf{D}} \mathbf{B}^M)$ as a target function to minimize. This topic will be discussed in more detail in Section IV.

IV. SAMPLING THEORY IN THE GLCT DOMAIN

In this section, we present a novel sampling theory for the GLCT, drawing inspiration from the established sampling theories of the GFT and the GFRFT [13]–[16], [35]. Our approach to graph sampling, rooted in the graph linear canonical basis and graph frequency-based sampling methods, tackles the challenge of reconstructing bandlimited graph signals from their subsampled counterparts.

An M -bandlimited graph signal is characterized as a signal with zero graph linear canonical coefficients aligned with the eigenvalues of $\lambda_{|\mathcal{F}|-1}$. This definition implies that $f(i) = 0$ for $\lambda, i \geq |\mathcal{F}|$, where \mathcal{F} denotes the set of indices associated with non-zero graph linear canonical coefficients.

Specifically, the indices in \mathcal{F} identify those components of the graph linear canonical coefficients that contribute significantly to the signal. We further elaborate on the concept of M -bandlimited graph signals in the subsequent discussion.

A. M -Bandlimited Graph Signals

In the context of GSP, the notion of M -bandlimited signals becomes imperative, necessitating adherence to the previously introduced conditions of perfect localization. Assuming an arbitrary signal \mathbf{y} lacks bandlimited characteristics, preprocessing is required in the form of bandlimiting.

This involves the utilization of a graph spectral domain filter $\Sigma_{\mathcal{F}}$, defined analogously to Eq. (10). First, the GLCT is applied to the signal \mathbf{y} , yielding $\hat{\mathbf{y}} = \mathbf{O}^M \mathbf{y}$. Subsequently, $\hat{\mathbf{y}}$ undergoes filtering

$$\hat{\mathbf{x}} = \Sigma_{\mathcal{F}} \hat{\mathbf{y}} = \text{diag}(1, \dots, 1) \hat{\mathbf{y}}.$$

Following this, an IGLCT is applied to $\hat{\mathbf{x}}$, resulting in $\mathbf{x} = \mathbf{O}^{-M} \hat{\mathbf{x}}$. Consolidating these steps, we arrive at

$$\mathbf{x} = \mathbf{O}^{-M} \Sigma_{\mathcal{F}} \mathbf{O}^M \mathbf{y}, \quad (20)$$

where, it is discernible that $\mathbf{O}^{-M} \Sigma_{\mathcal{F}} \mathbf{O}^M = \mathbf{B}^M$. Through this methodology, an M -bandlimited signal \mathbf{x} is attained, satisfying the conditions of perfect localization as delineated in Eqs. (11) and (12). Therefore, we introduce the following definition for the M -bandlimited set.

Definition 2. The closed subspace of graph signals in \mathbb{C}^N with a bandwidth of at most $|\mathcal{F}|$ is denoted as $\text{BL}_{|\mathcal{F}|}(\mathbf{O}^M)$, where \mathbf{O}^M is defined as in Eq. (2).

B. Sampling and Perfect Recovery

We initiate our exploration by addressing the fundamental challenge of determining conditions and methodologies for the perfect recovery of \mathbf{x} from the sampled graph signal $\mathbf{x}_{\mathcal{S}}$. Drawing upon certain definitions of graph signal sampling outlined in the preliminaries, we present the following theorem, mirroring the principles introduced in [13].

Theorem 2. Let $\mathbf{D} \in \mathbb{C}^{|\mathcal{S}| \times N}$ denote the sampling operator. The interpolation (recovery) operator $\mathbf{R} \in \mathbb{C}^{N \times |\mathcal{S}|}$ is characterized by the following conditions: (1) \mathbf{R} spans the space $\text{BL}_{|\mathcal{F}|}(\mathbf{O}^M)$; (2) $\mathbf{R}\mathbf{D}$ functions as a projection operator, achieving perfect recovery

$$\mathbf{x} = \mathbf{R}\mathbf{D}\mathbf{x} = \mathbf{R}\mathbf{x}_{\mathcal{S}}, \quad \text{for all } \mathbf{x} \in \text{BL}_{|\mathcal{F}|}(\mathbf{O}^M), \quad (21)$$

where $\mathbf{x}_{\mathcal{S}}$ denotes the sampled graph signal.

If the original signal \mathbf{x} can be perfectly recovered, then

$$\mathbf{x} - \mathbf{R}\mathbf{D}\mathbf{x} = \mathbf{x} - \mathbf{R}(\mathbf{I} - \bar{\mathbf{D}})\mathbf{x} = \mathbf{x} - \mathbf{R}(\mathbf{I} - \bar{\mathbf{D}}\mathbf{B}^M)\mathbf{x}.$$

Hence, the matrix $\mathbf{R} = (\mathbf{I} - \bar{\mathbf{D}}\mathbf{B}^M)^{-1}$. The perfect recoverability of \mathbf{x} implies the existence of \mathbf{R} , which is tantamount to the invertibility of $(\mathbf{I} - \bar{\mathbf{D}}\mathbf{B}^M)$. Consequently, we infer that when $\|\bar{\mathbf{D}}\mathbf{B}^M\| < 1$, the original signal can be perfectly recovered, as reported in [14]. Herein, the maximum norm of $\bar{\mathbf{D}}\mathbf{B}^M$ being 1 restricts our consideration to this scenario, where perfect localization on the complement of the sampling set prevails, rendering signal recovery unattainable. This is closely related to the uncertainty principles discussed in Section III. Furthermore, since $\mathbf{x} \in \text{BL}_{|\mathcal{F}|}(\mathbf{O}^M)$,

$$(\mathbf{I} - \bar{\mathbf{D}}\mathbf{B}^M)\mathbf{x} = (\mathbf{I} - \bar{\mathbf{D}})\mathbf{x} = \mathbf{D}\mathbf{x} = \mathbf{D}\mathbf{B}^M\mathbf{x}.$$

By analyzing the preceding equation, it is evident that $(\mathbf{I} - \bar{\mathbf{D}}\mathbf{B}^{\mathbf{M}})$ is equivalent to $\mathbf{D}\mathbf{B}^{\mathbf{M}}$, leading to the conclusion that $\mathbf{R} = (\mathbf{D}\mathbf{B}^{\mathbf{M}})^{-1}$. However, in the case of a degenerate matrix, the rank of $\mathbf{D}\mathbf{B}^{\mathbf{M}}$ may be less than full. In such instances, we employ the pseudo-inverse to define $\mathbf{R} = (\mathbf{D}\mathbf{B}^{\mathbf{M}})^{\dagger}$.

We have the following theorem regarding sampling and perfect recovery.

Theorem 3. For \mathbf{D} such that

$$\text{rank}(\mathbf{D}\mathbf{O}_{|\mathcal{F}|}^{-\mathbf{M}}) = |\mathcal{F}|, \quad |\mathcal{F}| < N, \quad (22)$$

where $\mathbf{D}\mathbf{O}_{|\mathcal{F}|}^{-\mathbf{M}}$ denotes the first $|\mathcal{F}|$ columns of $\mathbf{D}\mathbf{O}^{-\mathbf{M}}$. For all $\mathbf{x} \in \text{BL}_{|\mathcal{F}|}(\mathbf{O}^{\mathbf{M}})$, perfect recovery, $\mathbf{x} = \mathbf{R}\mathbf{D}\mathbf{x}$, is achieved by choosing

$$\mathbf{R} = (\mathbf{D}\mathbf{B}^{\mathbf{M}})^{\dagger} = (\mathbf{D}\mathbf{O}^{-\mathbf{M}}\mathbf{\Sigma}_{\mathcal{F}}\mathbf{O}^{\mathbf{M}})^{\dagger} = \mathbf{O}_{|\mathcal{F}|}^{-\mathbf{M}}(\mathbf{D}\mathbf{O}_{|\mathcal{F}|}^{-\mathbf{M}})^{\dagger},$$

where let $\mathbf{P} = (\mathbf{D}\mathbf{O}_{|\mathcal{F}|}^{-\mathbf{M}})^{\dagger}$, thus $\mathbf{P}\mathbf{D}\mathbf{O}_{|\mathcal{F}|}^{-\mathbf{M}} = \mathbf{I}_{|\mathcal{F}| \times |\mathcal{F}|}$ is a $|\mathcal{F}| \times |\mathcal{F}|$ identity matrix.

Proof. Since $\text{rank}(\mathbf{D}\mathbf{O}_{|\mathcal{F}|}^{-\mathbf{M}}) = |\mathcal{F}|$ and $\text{rank}(\mathbf{P}\mathbf{D}\mathbf{O}_{|\mathcal{F}|}^{-\mathbf{M}}) = |\mathcal{F}|$, $\text{rank}(\mathbf{P}) = |\mathcal{F}|$, i.e. \mathbf{P} spans $\mathbb{C}^{|\mathcal{F}|}$. Hence, $\mathbf{R} = \mathbf{O}_{|\mathcal{F}|}^{-\mathbf{M}}\mathbf{P}$ spans $\text{BL}_{|\mathcal{F}|}(\mathbf{O}^{\mathbf{M}})$.

Let $\mathbf{J} = \mathbf{R}\mathbf{D}$, we have

$$\begin{aligned} \mathbf{J}^2 &= \mathbf{R}\mathbf{D}\mathbf{R}\mathbf{D} = \mathbf{O}_{|\mathcal{F}|}^{-\mathbf{M}}(\mathbf{P}\mathbf{D}\mathbf{O}_{|\mathcal{F}|}^{-\mathbf{M}})\mathbf{P}\mathbf{D} \\ &= (\mathbf{O}_{|\mathcal{F}|}^{-\mathbf{M}}\mathbf{I}_{|\mathcal{F}| \times |\mathcal{F}|}\mathbf{P})\mathbf{D} = \mathbf{R}\mathbf{D} = \mathbf{J}, \end{aligned}$$

thus $\mathbf{J} = \mathbf{P}\mathbf{D}$ is a projection operator.

Since $\mathbf{R}\mathbf{D}$ is a projection operator, $\mathbf{R}\mathbf{D}\mathbf{x}$ is an approximation of \mathbf{x} in the space of $\text{BL}_{|\mathcal{F}|}(\mathbf{O}^{\mathbf{M}})$. We achieve perfect recovery when \mathbf{x} is in the space of $\text{BL}_{|\mathcal{F}|}(\mathbf{O}^{\mathbf{M}})$. \square

Remark 2. When $|\mathcal{S}| < |\mathcal{F}|$, it holds that $\text{rank}(\mathbf{P}\mathbf{D}\mathbf{O}_{|\mathcal{F}|}^{-\mathbf{M}}) \leq \text{rank}(\mathbf{P}) \leq |\mathcal{S}| < |\mathcal{F}|$, thus rendering $\mathbf{P}\mathbf{D}\mathbf{O}_{|\mathcal{F}|}^{-\mathbf{M}}$ incapable of being an identity matrix, and perfect recovery of the original signal is unattainable. In the case of $|\mathcal{S}| = |\mathcal{F}|$, for $\mathbf{P}\mathbf{D}\mathbf{O}_{|\mathcal{F}|}^{-\mathbf{M}}$ to be the identity matrix, \mathbf{P} must be the inverse of $\mathbf{D}\mathbf{O}_{|\mathcal{F}|}^{-\mathbf{M}}$. For $|\mathcal{S}| > |\mathcal{F}|$, \mathbf{P} is the pseudo-inverse of $\mathbf{D}\mathbf{O}_{|\mathcal{F}|}^{-\mathbf{M}}$, and in cases where $|\mathcal{S}| \geq |\mathcal{F}|$, perfect recovery of the original signal is possible. For simplicity, we consider the scenario $|\mathcal{S}| = |\mathcal{F}|$.

C. Qualified Sampling Operator

The implications of **Theorem 3** underscore that achieving perfect recovery may be unattainable, even for \mathbf{M} -bandlimited graph signals, with arbitrary sampling operators. A qualified sampling operator must, at a minimum, select $|\mathcal{F}|$ linearly independent rows from within $\mathbf{O}_{|\mathcal{F}|}^{-\mathbf{M}}$. We will introduce the definition of a qualified sampling operator, ensuring its adherence to the conditions delineated in **Theorem 3**. To achieve this, we formally define the adjacency matrix in the graph linear canonical domain, thus

$$\mathbf{A}^{\mathbf{M}} = \mathbf{O}^{-\mathbf{M}}\mathbf{\Lambda}_{\mathbf{A}}\mathbf{O}^{\mathbf{M}}, \quad (23)$$

where $\mathbf{A}^{\mathbf{M}}$ lacks physical significance as it represents a complex matrix, specifically the adjacency matrix. However,

when $\mathbf{M} = (0, 1; -1, 0)$, $\mathbf{O}^{\mathbf{M}}$ degenerates into \mathbf{V}^{-1} , and in this case, $\mathbf{A}^{\mathbf{M}}$ serves as the shift operator.

For any sampling and recovery operators satisfying **Theorem 3**, when \mathbf{x} is \mathbf{M} -bandlimited, we have

$$\mathbf{x} = \mathbf{R}\mathbf{D}\mathbf{x} = \mathbf{O}_{|\mathcal{F}|}^{-\mathbf{M}}\mathbf{P}\mathbf{x}_{\mathcal{S}} = \mathbf{O}_{|\mathcal{F}|}^{-\mathbf{M}}\hat{\mathbf{x}}_{|\mathcal{F}|},$$

where $\hat{\mathbf{x}}_{|\mathcal{F}|}$ represents the first $|\mathcal{F}|$ values of $\hat{\mathbf{x}}$. Therefore, we derive

$$\mathbf{x}_{\mathcal{S}} = \mathbf{P}^{-1}\hat{\mathbf{x}}_{|\mathcal{F}|} = \mathbf{P}^{-1}\hat{\mathbf{x}}_{\mathcal{S}}.$$

As observed, the sampled signal $\mathbf{x}_{\mathcal{S}}$ and the frequency signal $\hat{\mathbf{x}}_{|\mathcal{F}|}$ in the dual domain form a graph linear canonical operator. Therefore, we obtain a new adjacency matrix, leading to the following theorem similar to [13].

Theorem 4. For $\mathbf{x} \in \text{BL}_{|\mathcal{F}|}(\mathbf{O}^{\mathbf{M}})$, where $|\mathcal{S}| = |\mathcal{F}|$, and if \mathbf{D} is a qualified sampling operator, then

$$\mathbf{A}_{\mathcal{S}}^{\mathbf{M}} = \mathbf{P}^{-1}\mathbf{\Lambda}_{\mathbf{A}_{|\mathcal{F}|}}\mathbf{P} \in \mathbb{C}^{|\mathcal{F}| \times |\mathcal{F}|}, \quad (24)$$

where $\mathbf{P} = (\mathbf{D}\mathbf{O}_{|\mathcal{F}|}^{-\mathbf{M}})^{-1}$, and $\mathbf{\Lambda}_{\mathbf{A}_{|\mathcal{F}|}}$ is the diagonal matrix of the first $|\mathcal{F}|$ eigenvalues of $\mathbf{\Lambda}_{\mathbf{A}}$.

In the graph linear canonical domain, $\mathbf{A}_{\mathcal{S}}^{\mathbf{M}}$ is obtained through $\mathbf{A}^{\mathbf{M}}$ sampling. The original graph signal \mathbf{x} and the sampled graph signal $\mathbf{x}_{\mathcal{S}}$ have equivalent frequency content after undergoing the corresponding GLCT. The information preserved by $\mathbf{A}_{\mathcal{S}}^{\mathbf{M}}$ can be expressed as follows

$$\begin{aligned} \mathbf{x}_{\mathcal{S}} - \mathbf{A}_{\mathcal{S}}^{\mathbf{M}}\mathbf{x}_{\mathcal{S}} &= \mathbf{P}^{-1}\hat{\mathbf{x}}_{\mathcal{S}} - \mathbf{P}^{-1}\mathbf{\Lambda}_{\mathbf{A}_{|\mathcal{F}|}}\mathbf{P}\mathbf{P}^{-1}\hat{\mathbf{x}}_{\mathcal{S}} \\ &= \mathbf{P}^{-1}(\hat{\mathbf{x}}_{\mathcal{S}} - \mathbf{\Lambda}_{\mathbf{A}_{|\mathcal{F}|}}\hat{\mathbf{x}}_{\mathcal{S}}) \\ &= \mathbf{D}\mathbf{O}_{|\mathcal{F}|}^{-\mathbf{M}}(\mathbf{I} - \mathbf{\Lambda}_{\mathbf{A}_{|\mathcal{F}|}})\mathbf{O}_{|\mathcal{F}|}^{\mathbf{M}}\mathbf{x} \\ &= \mathbf{D}(\mathbf{x} - \mathbf{A}^{\mathbf{M}}\mathbf{x}), \end{aligned}$$

where, $\mathbf{x} \in \text{BL}_{|\mathcal{F}|}(\mathbf{O}^{\mathbf{M}})$, and $\hat{\mathbf{x}}_{|\mathcal{F}|} = \hat{\mathbf{x}}_{\mathcal{S}}$.

By reordering and rearranging the eigenvalues in the matrix of the GLCT, **Theorem 4** applies to all graph signals that are \mathbf{M} -bandlimited in the GLCT domain.

D. Optimal Sampling Operator

When sampling graph signals, aside from determining the appropriate sample size, devising a strategy for selecting sampling node locations is crucial as the positions of the sampled nodes play a pivotal role in the performance of the reconstruction algorithm. Given the multiple choices of $|\mathcal{F}|$ linearly independent rows in $\mathbf{O}_{|\mathcal{F}|}^{-\mathbf{M}}$, our objective is to opt for an optimal set that minimizes the impact of noise. One strategy involves selecting sampling positions to minimize the normalized MSE (NMSE) [14], [35]. Consider the noise e introduced during the sampling process

$$\mathbf{x}_{\mathcal{S}} = \mathbf{D}\mathbf{x} + e,$$

where \mathbf{D} is qualified. The recovered signal $\mathbf{x}_{\mathcal{R}}$ is then given by

$$\mathbf{x}_{\mathcal{R}} = \mathbf{R}\mathbf{x}_{\mathcal{S}} = \mathbf{R}\mathbf{D}\mathbf{x} + \mathbf{R}e = \mathbf{x} + \mathbf{R}e.$$

Consequently, the bound of the recovery error, obtained through the norm and Cauchy-Schwarz inequality, is

$$\|\mathbf{x}_{\mathcal{R}} - \mathbf{x}\|_2 = \|\mathbf{R}e\|_2 = \|\mathbf{O}_{|\mathcal{F}|}^{-\mathbf{M}}\mathbf{P}e\|_2 \leq \|\mathbf{O}_{|\mathcal{F}|}^{-\mathbf{M}}\|_2\|\mathbf{P}\|_2\|e\|_2.$$

Given that $\|\mathbf{O}_{|\mathcal{F}|}^{-\mathbf{M}}\|_2$ and $\|e\|_2$ are fixed, the objective is to minimize the spectral norm of \mathbf{P} , which is the pseudo-inverse of $\mathbf{D}\mathbf{O}_{|\mathcal{F}|}^{-\mathbf{M}}$. The norm considered here can be either the 2-norm or the Frobenius norm. The optimal norm is selected based on optimization algorithms and numerical methods.

In the following, we provide several alternative strategies for selecting sampling sets in the GLCT domain based on the approach proposed by [13]–[15].

1) *Minimization of the Frobenius Norm of \mathbf{P} (MinFro)*

In this strategy, the objective is to directly minimize the Frobenius norm of the matrix \mathbf{P} , aiming to minimize the NMSE between the original and recovery signals. The method involves selecting columns from the matrix $\mathbf{O}_{|\mathcal{F}|}^{-\mathbf{M}}$ to minimize the Frobenius norm of the pseudo-inverse matrix \mathbf{P} ,

$$\mathbf{D}^{\text{opt}} = \arg \min_{\mathbf{D}} \|\mathbf{P}\|_F = \arg \min_{\mathbf{D}} \|\Sigma_{\mathcal{F}} \mathbf{O}^{\mathbf{M}} \mathbf{D}\|_F. \quad (25)$$

2) *Minimization of the singular value of \mathbf{P} (MinPinv)*

Due to $\lambda_i(\mathbf{B}^{\mathbf{M}} \mathbf{D} \mathbf{B}^{\mathbf{M}}) = \sigma_i^2(\mathbf{B}^{\mathbf{M}} \mathbf{D}) = \sigma_i^2(\Sigma_{\mathcal{F}} \mathbf{O}^{\mathbf{M}} \mathbf{D}) = \sigma_i^2(\mathbf{P})$, similar to 1), in the case of uncorrelated noise, this is equivalent to minimizing $\sum_i^{|\mathcal{F}|} \sigma_i^2$,

$$\mathbf{D}^{\text{opt}} = \arg \min_{\mathbf{D}} \sum_{i=1}^{|\mathcal{F}|} \sigma_i^2(\mathbf{P}). \quad (26)$$

3) *Maximization of the singular value of $\mathbf{D}\mathbf{O}_{|\mathcal{F}|}^{-\mathbf{M}}$ (MaxSig)*

The third strategy aims to select columns of the matrix $\mathbf{O}_{|\mathcal{F}|}^{-\mathbf{M}}$ to maximize its singular values. Although this strategy is not directly related to NMSE optimization, it is easy to implement and demonstrates good performance in practice,

$$\mathbf{D}^{\text{opt}} = \arg \max_{\mathbf{D}} \sum_{i=1}^{|\mathcal{F}|} \sigma_i^2(\mathbf{D}\mathbf{O}_{|\mathcal{F}|}^{-\mathbf{M}}). \quad (27)$$

4) *Maximization of the minimum singular value of $\mathbf{D}\mathbf{O}_{|\mathcal{F}|}^{-\mathbf{M}}$ (MaxSigMin)*

The fourth strategy is designed to leverage the 2-norm to minimize NMSE, which is equivalent to minimizing the largest singular value of \mathbf{P} . In other words, we aim to maximize the smallest singular value σ_{\min} of $\mathbf{D}\mathbf{O}_{|\mathcal{F}|}^{-\mathbf{M}}$ for every qualified \mathbf{D} ,

$$\mathbf{D}^{\text{opt}} = \arg \max_{\mathbf{D}} \sigma_{\min}(\mathbf{D}\mathbf{O}_{|\mathcal{F}|}^{-\mathbf{M}}). \quad (28)$$

5) *Maximization of the Volume of the Parallelepiped Formed With the Columns of $\mathbf{O}_{|\mathcal{F}|}^{-\mathbf{M}}$ (MaxVol)*

This strategy, inspired by [14], aims to select a set \mathcal{S} of columns from the matrix $\mathbf{O}_{|\mathcal{F}|}^{-\mathbf{M}}$ to maximize the volume of the parallelepiped constructed with the chosen columns. Essentially, this approach involves completing the matrix $\mathbf{O}_{|\mathcal{F}|}^{-\mathbf{M}}$. The volume can be computed as the determinant of the matrix $\mathbf{O}_{|\mathcal{F}|}^{\mathbf{M}} \mathbf{D}\mathbf{O}_{|\mathcal{F}|}^{-\mathbf{M}}$.

$$\mathbf{D}^{\text{opt}} = \arg \max_{\mathbf{D}} \prod_{i=1}^{|\mathcal{F}|} \lambda_i \left(\mathbf{O}_{|\mathcal{F}|}^{\mathbf{M}} \mathbf{D}\mathbf{O}_{|\mathcal{F}|}^{-\mathbf{M}} \right). \quad (29)$$

We propose five greedy methods to solve this selection problem and obtain the *optimal sampling operator*. Since strategies 1), 2), and 3) are essentially consistent, we give algorithms 1, 2, and 3 below that summarize the three sampling strategies 2), 4), and 5).

Algorithm 1 Optimal Sampling Operator based on MinPinv

Input

$\mathbf{O}_{|\mathcal{F}|}^{-\mathbf{M}}$ the first $|\mathcal{F}|$ columns of $\mathbf{O}^{-\mathbf{M}}$
 $|\mathcal{S}|$ the number of samples
 N the number of rows in $\mathbf{O}_{|\mathcal{F}|}^{-\mathbf{M}}$

Output

\mathcal{S} sampling set

Function

```

for  $k = 1 : |\mathcal{S}|$ 
     $s = \arg \min_{j \in \{1:N\} - \mathcal{S}} \sum_{i=1}^{|\mathcal{F}|} \frac{1}{\sigma_i^2 \left( \left( \mathbf{O}_{|\mathcal{F}|}^{-\mathbf{M}} \right)_{\mathcal{S} \cup \{j\}} \right)}$ 
     $\mathcal{S} = \mathcal{S} + \{s\}$ 
end
return  $\mathcal{S}$ 

```

Algorithm 2 Optimal Sampling Operator based on MaxSigMin

Input

$\mathbf{O}_{|\mathcal{F}|}^{-\mathbf{M}}$ the first $|\mathcal{F}|$ columns of $\mathbf{O}^{-\mathbf{M}}$
 $|\mathcal{S}|$ the number of samples
 N the number of rows in $\mathbf{O}_{|\mathcal{F}|}^{-\mathbf{M}}$

Output

\mathcal{S} sampling set

Function

```

for  $k = 1 : |\mathcal{S}|$ 
     $s = \arg \max_{j \in \{1:N\} - \mathcal{S}} \sigma_{\min} \left( \left( \mathbf{O}_{|\mathcal{F}|}^{-\mathbf{M}} \right)_{\mathcal{S} + \{j\}} \right)$ 
     $\mathcal{S} = \mathcal{S} + \{s\}$ 
end
return  $\mathcal{S}$ 

```

Algorithm 3 Optimal Sampling Operator based on MaxVol

Input

$\mathbf{O}_{|\mathcal{F}|}^{-\mathbf{M}}$ the first $|\mathcal{F}|$ columns of $\mathbf{O}^{-\mathbf{M}}$
 $|\mathcal{S}|$ the number of samples
 N the number of rows in $\mathbf{O}_{|\mathcal{F}|}^{-\mathbf{M}}$

Output

\mathcal{S} sampling set

Function

```

for  $k = 1 : |\mathcal{S}|$ 
     $s = \arg \max_{j \in \{1:N\} - \mathcal{S}} \prod_{i=1}^{|\mathcal{F}|} \lambda_i \left( \left( \left( \mathbf{O}_{|\mathcal{F}|}^{-\mathbf{M}} \right)^*_{\mathcal{S} \cup \{j\}} \left( \mathbf{O}_{|\mathcal{F}|}^{-\mathbf{M}} \right)_{\mathcal{S} \cup \{j\}} \right) \right)$ 
     $\mathcal{S} = \mathcal{S} + \{s\}$ 
end
return  $\mathcal{S}$ 

```

We compared our proposed five sampling strategies with random sampling. As shown in Fig. 2, the NMSE is reported, defined as the error between the original and recovered signals divided by the original signal for each node. (a) is based on a cycle graph with $N = 32$ nodes, and the signal is an M-bandlimited signal with parameters $\alpha = 0.8, \sigma = 32, \xi = 0.5k + 1, k = 1, \dots, N$. The frequency bandwidth is $|\mathcal{F}| = 4$. (b) is based on a Swiss roll graph with $N = 256$ nodes, and the signal is an M-bandlimited signal with the same parameters. The frequency bandwidth is $|\mathcal{F}| = 32$. We compare the NMSE of six sampling methods as the number of sampled nodes increases for two different graph signals. We observed that, with a small number of sampling nodes, all methods except random sampling could effectively recover the signal.

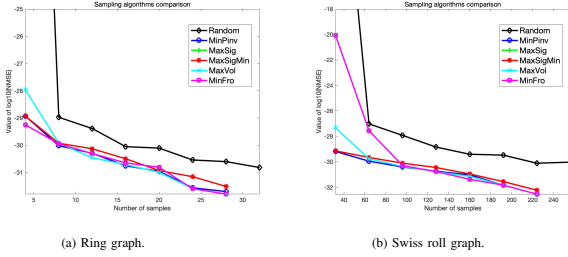


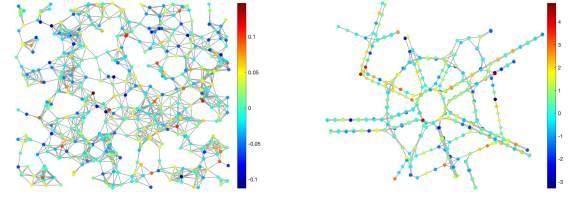
Fig. 2: NMSE vs. number of samples for different sampling strategies.

V. APPLICATIONS AND NUMERICAL EXPERIMENTS

In this section, we conduct simulation experiments and test GLCT sampling and recovery in a semi-supervised classification application [35] and clustering of bus test cases [37]. Semi-supervised classification seeks to categorize a vast dataset with the assistance of a limited number of labeled instances. In the context of GSP, the smoothness of labels across the graph can be observed through low-pass characteristics in the graph spectral domain. Simultaneously, in the case of the bus test case with 118 nodes, the generator dynamically produces smooth graph signals, justifying the validity of the M-bandlimited assumption. We utilize three frameworks (GFT sampling, GFRFT sampling, and GLCT sampling) for GSP, comparing the NMSE of graph signal recovery and the accuracy of the applied classification.

A. Simulations

We conducted simulations using the graph signal processing toolbox (GSPBox) in MATLAB [38] for two examples. The first example involves a David sensor network with $N = 500$ nodes. We set the bandwidth $|\mathcal{F}| = 60$, and the M-bandlimited parameters to $\alpha = 0.7, \sigma = N/2, \xi = 0.5k + 0.5, k = 1, \dots, N$. The graph signal is the real part of $\mathbf{x} = \text{real}(\mathbf{f}_1 + 0.5\mathbf{f}_2 + \mathbf{f}_3)$ obtained through M-bandlimited operation, where \mathbf{f}_i represents the i -th column of \mathbf{O}^{-M} . The second example involves the vehicular traffic data in Rome. We set the bandwidth $|\mathcal{F}| = 50$, and the M-bandlimited parameters to $\alpha = 0.9, \sigma = N, \xi = 0.5k + 0.7, k = 1, \dots, N$. The graph signal is the real vehicular traffic data in Rome [39] obtained through M-bandlimited operation. The original graph signals are depicted in Fig. 3.



(a) Example 1: 500-node David sensor network graph. (b) Example 2: Roman vehicular traffic data graph.

Fig. 3: Original graph signal.

For both examples, we performed sampling and recovery of the graph signals using three optimal sampling operators based on MinPinv, corresponding to the GFT, α -order GFRFT, and M-matrix GLCT. The accuracy of the recovery was measured using the NMSE. Fig. 4 illustrates the locations of sampled nodes. The number of sampled nodes is 60 for (a), (b), and (c), and 50 for (e), (f), and (g). Fig. 5 displays the signals recovered through GFT sampling in (a) and (d), GFRFT sampling in (b) and (e), and GLCT sampling in (c) and (f). The NMSE for the three sampling frameworks applied to the two types of graph signals is presented in Table I. It is evident that GFT and GFRFT sampling fail to perfectly recover the graph signals, as these signals, while M-bandlimited, are not strictly bandlimited in the GFT and GFRFT domains. Only GLCT sampling achieves perfect signal recovery.

TABLE I: NMSE vs. different sampling frames for two examples.

	David sensor network	Roman vehicular traffic data
GFT sampling	1.6822	1.0038
GFRFT sampling	1.5754	1.0031
GLCT sampling	5.4518×10^{-25}	1.3541×10^{-25}

B. Classifying Online Blogs

In this section, we classify the political blog dataset with $N = 1224$ into conservative or liberal categories [40]. Nodes in the graph represent blogs, and edges represent hyperlinks between blogs. The label signal is set to 0 for conservative and 1 for liberal. The label signal spans the entire frequency band, and, as noted in [35], we know that the best results are achieved when the parameter α approaches 1. Therefore, while adjusting other parameters, we approximate the labeled signal using the lowest $|\mathcal{F}|$ fractional frequency components by solving the following optimization problem

$$\hat{\mathbf{x}}_{|\mathcal{F}|}^{\text{opt}} = \arg \min_{\hat{\mathbf{x}}_{|\mathcal{F}|} \in \mathbb{R}^{|\mathcal{F}|}} \left\| \text{thres} \left(\mathbf{D} \mathbf{O}_{|\mathcal{F}|}^{-M} \hat{\mathbf{x}}_{|\mathcal{F}|} \right) - \mathbf{x}_S \right\|_2^2, \quad (30)$$

where, the threshold function $\text{thres}(\cdot)$ assigns a value of 1 to all values greater than 0.5 and 0 otherwise. Subsequently, we set another threshold of 0.5 [13] to assign labels to the recovered signal

$$\mathbf{x}^{\text{opt}} = \text{thres} \left(\mathbf{O}_{|\mathcal{F}|}^{-M} \hat{\mathbf{x}}_{|\mathcal{F}|}^{\text{opt}} \right). \quad (31)$$

In our previous work [29], the parameter ξ only influenced the real and imaginary components of the spectrum, while

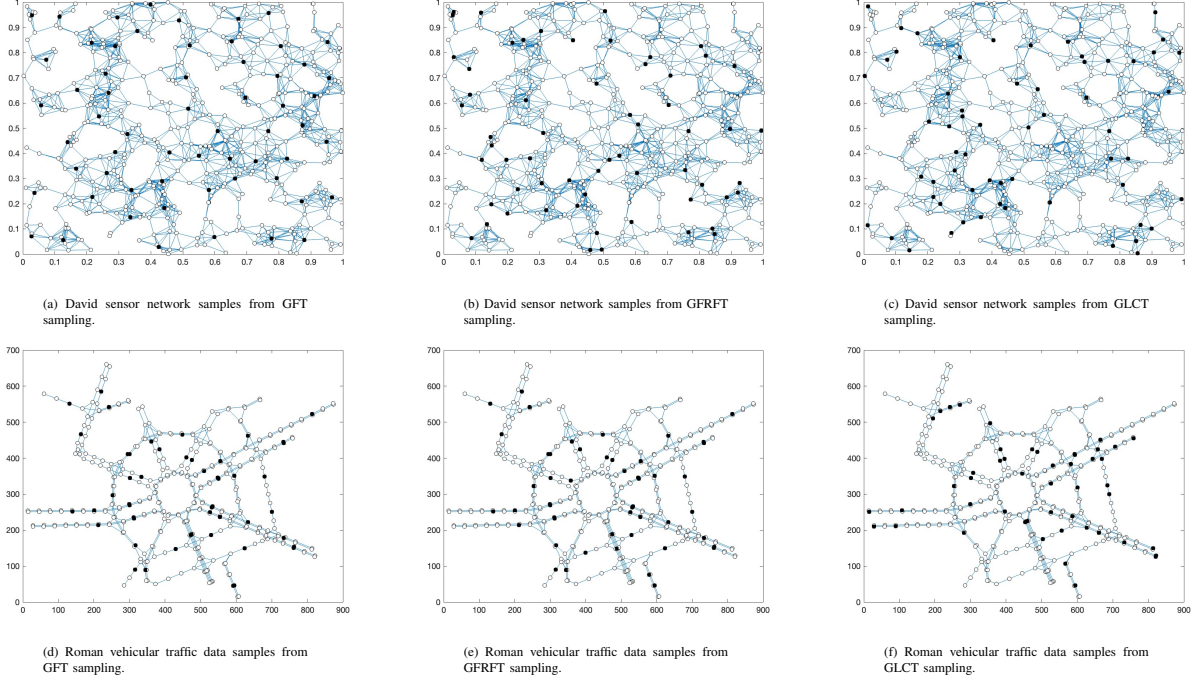


Fig. 4: The location of the sampled signals.

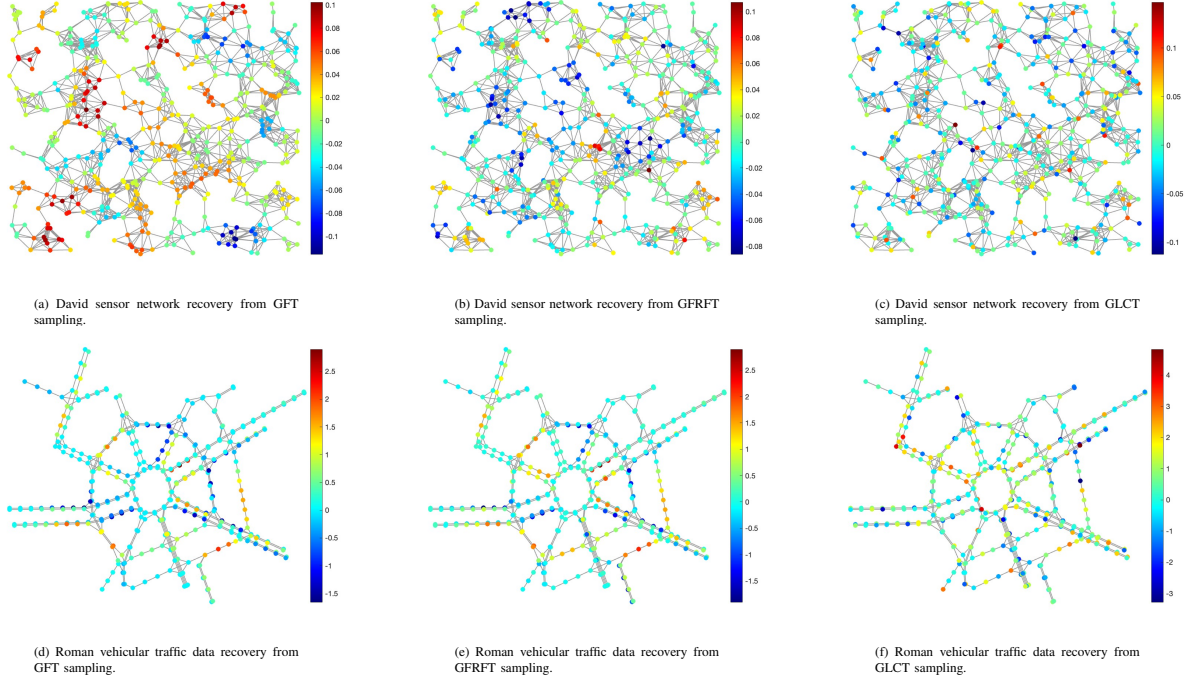


Fig. 5: Recovered graph signals.

the absolute value of the overall signal remained unchanged. Thus, we set $\xi = 0.5k + 1, k = 1, \dots, N$ in this study. We varied the parameter α from 0.99 to 1. For the parameter $\sigma = m \times 2^n, n \in \mathbb{R}$, as the accuracy remains constant when m is fixed, we considered variations in m , setting $m = 1, 3, 5, N$. Fig. 6(a) illustrates the change in classification accuracy for nodes with a frequency bandwidth $|\mathcal{F}| = 2$ and a sampling

size $M = 5$ as we vary the parameter α . The accuracy reaches its maximum value of 94.6078% when $\alpha = 0.995$ and $\sigma = 2^n$. In Fig. 6(b), the classification accuracy comparison is shown as the sampling size M changes for GFT, GFRFT from [35], and the optimal GLCT sampling. The GLCT outperforms the GFRFT and the GFT across varying sampling sizes M .

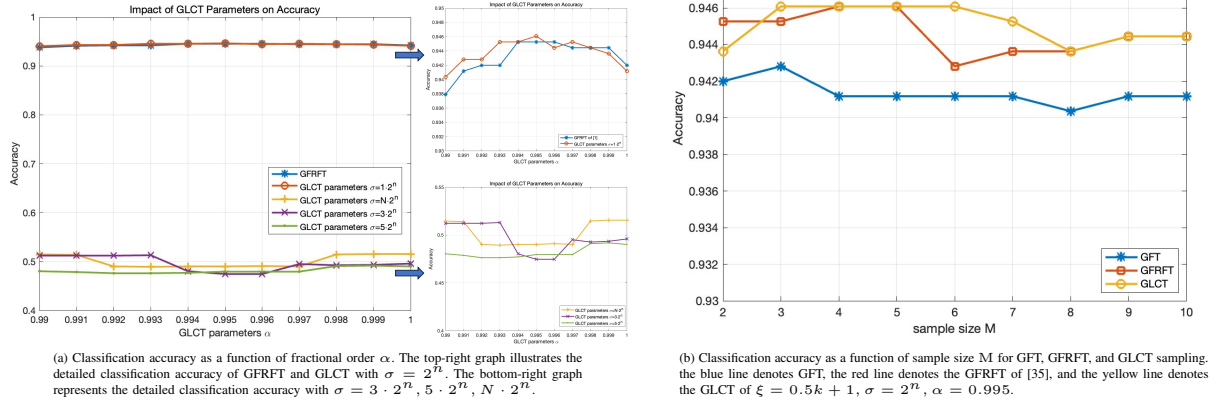


Fig. 6: Classification of online political blogs.

C. Clustering of Bus Test Case

The second part involves the application to a real-world network: the IEEE 118 bus test case, representing a portion of the U.S. power system as of December 1962 [37]. This graph comprises 118 nodes, with dynamic generation of smooth graph signals from power generators, making the bandlimited assumption reasonable. We consider a graph spectral bandwidth of $|\mathcal{F}| = 8$ and graph signal is the N th column of \mathbf{O}^M . We calculate the number of triangles in the graph, select different GLCT parameters for optimal sampling, and perform K -means clustering [41]. Finally, we evaluate the clustering results using

$$\text{Silhouette Score} = \frac{b(i) - a(i)}{\max\{a(i), b(i)\}},$$

where, $a(i)$ represents the average distance of sample i to other samples within the same cluster (intra-cluster compactness), and $b(i)$ represents the average distance of sample i to the nearest samples in other clusters (inter-cluster separation). A result closer to 1 indicates that samples are correctly assigned to clusters, with good separation between clusters.

Fig. 7(a) displays the silhouette score of sampling $M = |\mathcal{F}| = 8$ nodes with varying parameter α . The silhouette score reaches its maximum value of 0.8753 when $\xi = 0, \sigma = 2$ and, $\alpha = 1$. In (b), we compare the silhouette score of the GFRFT of $\alpha = 1$ (GFT), and the GLCT of $\xi = 0, \sigma = 2, \alpha = 1$ as M varies. Overall, the GLCT exhibits superior performance.

VI. CONCLUSION

In this paper, we propose the uncertainty principle and sampling theory in the GLCT domain. We demonstrate that the uncertainty principle in the GLCT domain has a broader scope compared to the GFT domain and shares interesting connections with sampling theory. We show that M -bandlimited graph signals in the GLCT domain can achieve perfect recovery through the GLCT with M matrix coefficients. We employ experimentally designed optimal sampling strategies to ensure perfect recovery while maximizing robustness against noise.

Various proposed sampling strategies are compared. Subsequently, we conduct simulation experiments and test GLCT sampling and recovery in a semi-supervised classification application and clustering of bus test cases. When comparing its performance with GFT and GFRFT sampling, we observe that GLCT sampling achieves superior classification accuracy under the optimal M matrix.

ACKNOWLEDGMENTS

This work were supported by the National Natural Science Foundation of China [No. 62171041], the BIT Research and Innovation Promoting Project [No.2023YCX053], and Beijing Municipal Natural Science Foundation [No. 4242011].

APPENDIX A PROOF OF LEMMA 1

The proof for this statement is available in [14]. By utilizing Eq. (11) and Eq. (12), we derive

$$\mathbf{B}^M \mathbf{D} \mathbf{B}^M \mathbf{x} = \mathbf{B}^M \mathbf{D} \mathbf{x} = \mathbf{B}^M \mathbf{x} = \mathbf{x}.$$

Consequently, $\lambda_{\max}(\mathbf{B}^M \mathbf{D} \mathbf{B}^M) = 1$. On the other hand, if $\mathbf{B}^M \mathbf{D} \mathbf{B}^M \mathbf{x} = \mathbf{x}$ is known, then $\mathbf{B}^M \mathbf{D} \mathbf{B}^M \mathbf{x} = \mathbf{B}^M \mathbf{x}$, as $(\mathbf{B}^M)^2 = \mathbf{B}^M$. This further implies $\mathbf{B}^M \mathbf{x} = \mathbf{x}$. Regarding vertex localization, utilizing the Rayleigh-Ritz theorem, we obtain

$$\max_{\mathbf{x}} \frac{\mathbf{x}^* \mathbf{D} \mathbf{x}}{\mathbf{x}^* \mathbf{x}} = \max_{\mathbf{x}} \frac{\mathbf{x}^* \mathbf{B}^{-M} \mathbf{D} \mathbf{B}^M \mathbf{x}}{\mathbf{x}^* \mathbf{x}} = 1.$$

Therefore, $\mathbf{D} \mathbf{x} = \mathbf{x}$, indicating perfect localization in both the vertex and spectral domains.

APPENDIX B PROOF OF LEMMA 2

The proof of this bound requires the use of curves [23]

$$\gamma(\zeta) := \left((\zeta \lambda_{\max})^{\frac{1}{2}} + ((1 - \zeta)(1 - \lambda_{\max}))^{\frac{1}{2}} \right)^2, \zeta \in [\lambda_{\max}, 1]. \quad (32)$$

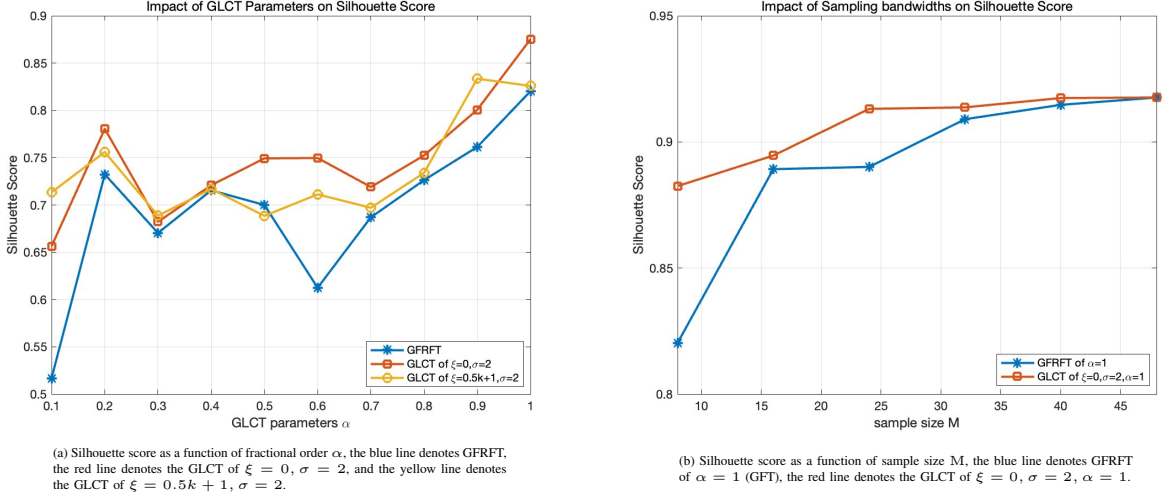


Fig. 7: Clustering of IEEE 118 Bus Test Case.

For a normalized vector signal \mathbf{x} , we consider two normalized vectors

$$\mathbf{y} = \frac{\mathbf{D}\mathbf{x}}{\|\mathbf{D}\mathbf{x}\|_2}, \text{ and } \mathbf{z} = \frac{\mathbf{B}^M\mathbf{x}}{\|\mathbf{B}^M\mathbf{x}\|_2}.$$

The usual definition of inner product $\langle \mathbf{y}, \mathbf{z} \rangle = \mathbf{y}^* \mathbf{z}$, angular distance is the measure of vectors on the unit sphere, we can define the angle distance between two vectors as

$$\angle(\mathbf{y}, \mathbf{z}) = \arccos \Re \langle \mathbf{y}, \mathbf{z} \rangle, \quad (33)$$

where, \angle denotes the angular distance, $\Re \langle \mathbf{y}, \mathbf{z} \rangle$ denotes the real number. In particular, the sum of the angular distances between vectors \mathbf{y} and \mathbf{x} , and \mathbf{z} and \mathbf{x} is always larger than the angular distance between \mathbf{y} and \mathbf{z} , i.e.

$$\arccos \Re \langle \mathbf{y}, \mathbf{x} \rangle + \arccos \Re \langle \mathbf{z}, \mathbf{x} \rangle \geq \arccos \Re \langle \mathbf{y}, \mathbf{z} \rangle. \quad (34)$$

For $\Re \langle \mathbf{y}, \mathbf{z} \rangle$, the upper bound is given by the Cauchy-Schwarz inequality

$$\begin{aligned} \Re \langle \mathbf{y}, \mathbf{z} \rangle &\leq |\Re \langle \mathbf{y}, \mathbf{z} \rangle| \leq |\langle \mathbf{y}, \mathbf{z} \rangle| \\ &= \frac{|\langle \mathbf{D}\mathbf{x}, \mathbf{B}^M\mathbf{x} \rangle|}{\|\mathbf{D}\mathbf{x}\|_2 \|\mathbf{B}^M\mathbf{x}\|_2} = \frac{|\langle \mathbf{D}^2\mathbf{x}, \mathbf{B}^M\mathbf{x} \rangle|}{\|\mathbf{D}\mathbf{x}\|_2 \|\mathbf{B}^M\mathbf{x}\|_2} \\ &= \frac{|\langle \mathbf{D}\mathbf{x}, \mathbf{D}\mathbf{B}^M\mathbf{x} \rangle|}{\|\mathbf{D}\mathbf{x}\|_2 \|\mathbf{B}^M\mathbf{x}\|_2} \leq \frac{\|\mathbf{D}\mathbf{x}\|_2 \|\mathbf{D}\mathbf{B}^M\mathbf{x}\|_2}{\|\mathbf{D}\mathbf{x}\|_2 \|\mathbf{B}^M\mathbf{x}\|_2} \\ &= \frac{\|\mathbf{D}\mathbf{x}\|_2 \sqrt{\langle \mathbf{D}^2\mathbf{B}^M\mathbf{x}, \mathbf{B}^M\mathbf{x} \rangle}}{\|\mathbf{D}\mathbf{x}\|_2 \|\mathbf{B}^M\mathbf{x}\|_2} \\ &= \frac{\|\mathbf{D}\mathbf{x}\|_2 \sqrt{\langle \mathbf{D}\mathbf{B}^M\mathbf{x}, (\mathbf{B}^M)^2\mathbf{x} \rangle}}{\|\mathbf{D}\mathbf{x}\|_2 \|\mathbf{B}^M\mathbf{x}\|_2} \\ &= \frac{\|\mathbf{D}\mathbf{x}\|_2 \sqrt{\langle \mathbf{B}^M\mathbf{D}\mathbf{B}^M\mathbf{x}, \mathbf{B}^M\mathbf{x} \rangle}}{\|\mathbf{D}\mathbf{x}\|_2 \|\mathbf{B}^M\mathbf{x}\|_2} \\ &\leq \frac{\|\mathbf{D}\mathbf{x}\|_2 \|\mathbf{B}^M\mathbf{x}\|_2 \|\mathbf{B}^M\mathbf{D}\mathbf{B}^M\mathbf{x}\|_2}{\|\mathbf{D}\mathbf{x}\|_2 \|\mathbf{B}^M\mathbf{x}\|_2} \\ &\leq \sqrt{\lambda_{\max}(\mathbf{B}^M\mathbf{D}\mathbf{B}^M)}. \end{aligned}$$

Since we assume that $\lambda_{\max} \leq \zeta^2 \eta^2$ and the right-hand expression in (34) is less than 1, we can get $\Re \langle \mathbf{y}, \mathbf{z} \rangle \leq \sqrt{\lambda_{\max}(\mathbf{B}^M\mathbf{D}\mathbf{B}^M)} \leq 1$, and $\Re \langle \mathbf{y}, \mathbf{x} \rangle = \zeta$, $\Re \langle \mathbf{z}, \mathbf{x} \rangle = \eta^M$.

So that formula (16) is proved. Next, we prove formula (17). Because the function $\arccos(x)$ decreases monotonically at $(0, 1]$, and according to formula (16), we get

$$\arccos \eta^M \geq \arccos \sqrt{\lambda_{\max}} - \arccos \zeta,$$

substituting both sides into the cosine function respectively

$$\eta^M \leq \cos \left(\arccos \sqrt{\lambda_{\max}} - \arccos \zeta \right).$$

Applying the trigonometric identity $\cos(a-b) = \cos a \cos b + \sin a \sin b$, we finally get the inequality

$$\eta^M \leq \sqrt{\lambda_{\max}} \zeta + \sqrt{1 - \lambda_{\max}} \sqrt{1 - \zeta^2}.$$

REFERENCES

- [1] D. I. Shuman, S. K. Narang, P. Frossard, A. Ortega, and P. Vandergheynst, "The emerging field of signal processing on graphs: Extending high-dimensional data analysis to networks and other irregular domains," *IEEE Signal Process. Mag.*, vol. 30, no. 3, pp. 83-98, 2013.
- [2] A. Sandryhaila and J. M. F. Moura, "Big data processing with signal processing on graphs: Representation and processing of massive data sets with irregular structure," *IEEE Signal Process. Mag.*, vol. 31, no. 5, pp. 80-90, 2014.
- [3] D. K. Hammond, P. Vandergheynst, and R. Gribonval, "Wavelets on graphs via spectral graph theory," *Appl. Comput. Harmon. Anal.*, vol. 30, no. 2, pp. 129-150, 2011.
- [4] A. Sandryhaila and J. M. F. Moura, "Discrete signal processing on graphs," *IEEE Trans. Signal Process.*, vol. 61, no. 7, pp. 1644-1656, 2013.
- [5] A. Ortega, P. Frossard, J. Kovačević, J. M. F. Moura, and P. Vandergheynst, "Graph signal processing: Overview, challenges, and applications," *Proc. IEEE*, vol. 106, no. 5, pp. 808-828, 2018.
- [6] G. Leus, A. G. Marques, J. M. F. Moura, A. Ortega and D. I. Shuman, "Graph signal processing: History, development, impact, and outlook," *IEEE Signal Process. Mag.*, vol. 40, no. 4, pp. 49-60, 2023.
- [7] S. Sardellitti, S. Barbarossa and P. D. Lorenzo, "On the graph Fourier transform for directed graphs," *IEEE J. Sel. Top. Signal Process.*, vol. 11, no. 6, pp. 796-811, 2017.
- [8] J. A. Deri and J. M. F. Moura, "Spectral projector-based graph Fourier transforms," *IEEE J. Sel. Top. Signal Process.*, vol. 11, no. 6, pp. 785-795, 2017.

- [9] A. Sandryhaila and J. M. F. Moura, "Discrete signal processing on graphs: Frequency analysis," *IEEE Trans. Signal Process.*, vol. 62, no. 12, pp. 3042-3054, 2014.
- [10] D. I. Shuman, B. Ricaud, and P. Vandergheynst, "Vertex-frequency analysis on graphs," *Appl. Comput. Harmon. Anal.*, vol. 40, no. 2, pp. 260-291, 2016.
- [11] M. W. Morency and G. Leus, "Graphon filters: Graph signal processing in the limit," *IEEE Trans. Signal Process.*, vol. 69, pp. 1740-1754, 2021.
- [12] Z. Yang, X. Zheng, Z. Yu and X. Li, "Graph filter design by ring-decomposition for 2-connected graphs," *Signal Process.*, vol. 201, 108725, 2022.
- [13] S. Chen, R. Varma, A. Sandryhaila, and J. Kovačević, "Discrete signal processing on graphs: Sampling theory," *IEEE Trans. Signal Process.*, vol. 63, no. 24, pp. 6510-6523, 2015.
- [14] M. Tsitsvero, S. Barbarossa and P. D. Lorenzo, "Signals on graphs: Uncertainty principle and sampling," *IEEE Trans. Signal Process.*, vol. 64, no. 18, pp. 4845-4860, 2016.
- [15] A. Sakiyama, Y. Tanaka, T. Tanaka, and A. Ortega, "Eigendecomposition-free sampling set selection for graph signals," *IEEE Trans. Signal Process.*, vol. 67, no. 10, pp. 2679-2692, 2019.
- [16] D. Y. Wei and Z. Yan, "Generalized sampling of graph signals with the prior information based on graph fractional Fourier transform," *Signal Process.*, vol. 214, 109263, 2024.
- [17] J. Shi and J. M. F. Moura, "Graph signal processing: Dualizing GSP sampling in the vertex and spectral domains," *IEEE Trans. Signal Process.*, vol. 70, pp. 2883-2898, 2022.
- [18] I. Zach, T. G. Dvorkind, and R. Talmon, "Graph signal interpolation and extrapolation over manifold of Gaussian mixture," *Signal Process.*, vol. 216, 109308, 2024.
- [19] S. Chen, A. Sandryhaila, J. M. F. Moura, and J. Kovačević, "Signal recovery on graphs: Variation minimization," *IEEE Trans. Signal Process.*, vol. 63, no. 17, pp. 4609-4624, 2015.
- [20] P. Berger, G. Hannak and G. Matz, "Graph signal recovery via primal-dual algorithms for total variation minimization," *IEEE J. Sel. Top. Signal Process.*, vol. 11, no. 6, pp. 842-855, 2017.
- [21] X. Wang, M. Wang and Y. Gu, "A distributed tracking algorithm for reconstruction of graph signals," *IEEE J. Sel. Top. Signal Process.*, vol. 9, no. 4, pp. 728-740, 2015.
- [22] A. Agaskar and Y. M. Lu, "A spectral graph uncertainty principle," *IEEE Trans. Inf. Theory*, vol. 59, no. 7, pp. 4338-4356, 2013.
- [23] W. Erb, "Shapes of uncertainty in spectral graph theory," *IEEE Trans. Inf. Theory*, vol. 67, no. 2, pp. 1291-1307, 2021.
- [24] L. L. Magoarou, R. Gribonval and N. Tremblay, "Approximate fast graph Fourier transforms via multilayer sparse approximations," *IEEE Trans. Signal Inf. Process. Netw.*, vol. 4, no. 2, pp. 407-420, 2018.
- [25] Y. Q. Wang, B. Z. Li, and Q. Y. Cheng, "The fractional Fourier transform on graphs," in *Proc. Asia-Pacific Signal Inf. Process. Assoc. Annu. Summit Conf. (APSIPA ASC)*, 2017, pp. 105-110.
- [26] Y. Zhang and B. Z. Li, "The fractional Fourier transform on graphs: Modulation and convolution," in *Proc. 8th IEEE Int. Conf. Signal Image Process. (ICSIP)*, 2023, pp. 737-741.
- [27] F. J. Yan and B. Z. Li, "Windowed fractional Fourier transform on graphs: Properties and fast algorithm," *Digit. Signal Process.*, vol. 118, 103210, 2021.
- [28] F. J. Yan and B. Z. Li, "Spectral graph fractional Fourier transform for directed graphs and its application," *Signal Process.*, vol. 210, 109099, 2023.
- [29] Y. Zhang and B. Z. Li, "Discrete linear canonical transform on graphs," *Digit. Signal Process.*, vol. 135, 103934, 2023.
- [30] H. M. Ozaktas, Z. Zalevsky, and M. A. Kutay, "The fractional Fourier transform with applications in optics and signal processing," *Wiley Sons*, Chichester, New York, 2001.
- [31] G. B. Folland and A. Sitaram, "The uncertainty principle: A mathematical survey," *J. Fourier Anal. Appl.* 3.3, pp. 207-238, 1997.
- [32] F. Ji and W. P. Tay, "A Hilbert space theory of generalized graph signal processing," *IEEE Trans. Signal Process.*, vol. 67, no. 24, pp. 6188-6203, 2019.
- [33] D. Slepian and H. O. Pollak, "Prolate spheroidal wave functions, Fourier analysis and uncertainty. I," *Bell Syst. Tech. J.*, vol. 40, no. 1, pp. 43-63, 1961.
- [34] H. J. Landau and H. O. Pollak, "Prolate spheroidal wave functions, Fourier analysis and uncertainty. II," *Bell Syst. Tech. J.*, vol. 40, no. 1, pp. 65-84, 1961.
- [35] Y. Q. Wang and B. Z. Li, "The fractional Fourier transform on graphs: Sampling and recovery," in *Proc. 14th IEEE Int. Conf. Signal Process. (ICSP)*, 2018, pp. 1103-1108.
- [36] M. Tsitsvero, S. Barbarossa, and P. D. Lorenzo, "Uncertainty principle and sampling of signals defined on graphs," in *Proc. 49th Asilomar Conf. Signals, Syst. Comput.*, 2015, pp. 1813-1818.
- [37] F. Pasqualetti, S. Zampieri, and F. Bullo, "Controllability metrics, limitations and algorithms for complex networks," *IEEE Trans. Control Netw. Syst.*, vol. 1, no. 1, pp. 40-52, 2014.
- [38] N. Perraudin, J. Paratte, D. Shuman, V. Kalofolias, P. Vandergheynst, and D. K. Hammond, "GSPBOX: a toolbox for signal processing on graphs," 2016, arXiv preprint, arXiv: 1408.5781.
- [39] P. D. Lorenzo, S. Barbarossa, and P. Banelli, "Sampling and recovery of graph signals," *Coop. Graph Signal Process.*, P. M. Djuric and C. Richard Eds. Elsevier, pp: 261-282, 2018.
- [40] L. A. Adamic and N. Glance, "The political blogosphere and the 2004 U.S. election: divided they blog," *Proc. LinkKDD*, pp. 35-43, 2005.
- [41] U. V. Luxburg, "A tutorial on spectral clustering," *Statist. Comput.*, vol. 17, no. 4, pp. 395-416, 2007.